MyD88 death domain oligomerisation determines Myddosome architecture: Implications for TLR signalling

Martin C. Moncrieffe[1,5] Daniel Bollschweiler[1], Bing Li[2], Pawel A. Penczek[3], Lee Hopkins[4], Clare E. Bryant[4], David Klenerman[2] and Nicholas J. Gay[1]

[1] Department of Biochemistry, University of Cambridge, Cambridge, CB2 1GA, UK.
[2] Department of Chemistry, University of Cambridge, Cambridge, CB2 1EW, UK.
[3] Department of Biochemistry & Molecular Biology, The University of Texas, McGovern Medical School, Houston, TX 77030, USA.
[4] Department of Veterinary Medicine, University of Cambridge, Cambridge, CB3 0ES, UK.

[5]Lead Contact
[1]Correspondence:mcm35@cam.ac.uk

SUMMARY

Toll like receptors (TLRs) are pivotal in triggering the innate immune response to pathogen infection. Ligand binding induces receptor dimerization which facilitates the recruitment of other post-receptor signal transducers into a complex signalosome, the Myddosome. Central to this process is Myeloid differentiation primary response 88 (MyD88) which is required by almost all TLRs and signalling is thought to proceed via the stepwise, sequential assembly of individual components. Here we show that the death domains of human MyD88 spontaneously and reversibly associate to form helical filaments *in vitro*. A 3.1 Å cryo-EM structure reveals that the architecture of the filament is identical to that of the MyD88-IRAK4-IRAK2 hetero-oligomeric Myddosome. Additionally, the death domain of IRAK4 interacts with the filaments to reconstitute the non-stoichiometric 6:4 MyD88-IRAK4 complex. Together, these data suggest that intracellularly, the MyD88 scaffold may be preformed and poised for recruitment of IRAKs on receptor activation and TIR engagement.

Keywords: TLR signaling, MyD88, Myddosome, IRAK, Cryo-EM, TIRFM, Light-sheet microscopy

INTRODUCTION

TLRs are pattern recognition receptors of the innate immune system that are activated when conserved molecular signatures on microbial or host molecules are detected (Akira, et al., 2006; Seong, et al., 2004). Architecturally, TLRs possess an extracellular ligand binding domain comprised of leucine rich repeats (LRRs), a single transmembrane segment and a cytosolic signalling domain which bears homology to the *D. melanogaster* protein Toll and the IL-1R receptor (TIR) (Gay, et al., 1991). A diverse number of disease states have been implicated with dysfunction in TLR signalling including autoimmune disorders (Fischer, et al., 2008), inflammation (Joosten, et al., 2016) and cancer (Chen, et al., 2008).

The human genome encodes ten TLRs and all, with the exception of TLR3 (Akira, et al., 2006), require the cytosolic adaptor human Myeloid differentiation primary response 88 (hMyD88). Signal transduction is thought to proceed sequentially by the stepwise assembly of proteins involved in the cascade initiated by ligand binding to the LRRs on the receptor ectodomain which leads to the formation of an activated receptor dimer. Receptor ectodomain dimerization facilitates association of its cytosolic TIR domains providing a scaffold for the recruitment of other TIR containing adaptor proteins, in particular, hMyD88 and MAL/TIRAP (Akira, et al., 2006; Gay, et al., 2014). hMyD88 also encodes an N-terminal death domain which is joined to the TIR by a linker region, the intermediate domain. *In vitro*, hMyD88 death domains ($hMyD88^{DD}$) assemble with the homologous domain on the IRAK kinases to produce an oligomeric structure, the Myddosome, which has an unusual stoichiometry of 6–8 hMyD88 subunits and precisely 4 each of IRAK4 and IRAK2 (Lin, et al., 2010; Motshwene, et al., 2009). A crystal structure of this complex reveals a left handed helical arrangement of death domains in which $hMyD88^{DD}$ forms two layers one of which interacts with IRAK4. IRAK2 then completes the ternary complex by associating with IRAK4 (Lin, et al., 2010). *In vivo* single molecule imaging data suggests that activated TLR receptor dimers nucleate the rapid assembly and disassembly of a Myddosome complex similar to that observed *in vitro* (Latty, et al., 2018).

Several TLRs require the PIP2 binding (Kagan, et al., 2006), TIR containing, membrane localised adaptor protein MAL/TIRAP for optimal signalling. A possible template for how interactions between receptor and

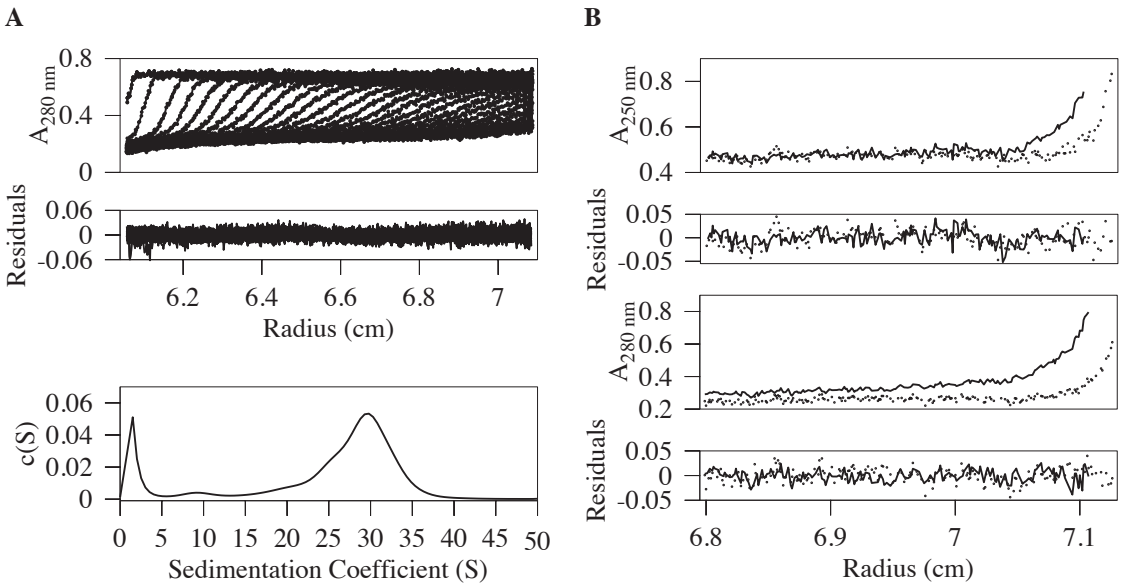

Figure 1 Sedimentation velocity and equilibrium measurement of the homo-oligomeric MyD88 death domain complex. Panel (**A**) shows velocity data, residuals after fitting and the c(S) distribution for the $hMyD88^{DD}$ death domain complex. The c(S) distribution is broad and has a peak at 30 S. (**B**) Sedimentation equilibrium data recorded at 250 nm and 280 nm and rotor speeds of 3000 and 4000 rpm. The recovered molecular weight of the $hMyD88^{DD}$ oligomer from a global analysis these data was 5.2 MDa.

adaptor TIRs nucleate Myddosome assembly has been obtained from the structure of the helical MAL^{TIR} filament (Ve, et al., 2017) which is assembled from protofilaments composed of parallel strands of MAL^{TIR} subunits held together by intra- and inter-strand interactions. In this model, the cytosolic TIR scaffold is helical and consists of intra-strand contacts between receptor TIRs. Adaptor TIRs, for example, those of $hMyD88^{TIR}$, are recruited sequentially to the receptor TIR scaffold by interstrand contacts (Ve, et al., 2017) followed by the recruitment of IRAK4 to hMyD88 via death domain interaction and subsequently by other members of the IRAK family whose phosphorylation drives downstream signalling events.

The stepwise sequential model is attractive because it explains known biochemical data and presents information flow during TLR signalling as a linear sequence of events in which signal propagation depends on the assembly of components from the preceding step. However, the model does not explain, for example, how the unusual stoichiometry of the Myddosome would arise by a stepwise assembly process. Additionally, the TIR domain of hMyD88 is envisaged to act as a nucleating hub (Latty, et al., 2018; Ve, et al., 2017; Vyncke, et al., 2016) which facilitates the oligomerisation of $hMyD88^{DD}$ observed in the Myddosome (Lin, et al., 2010; Motshwene, et al., 2009).

In this manuscript we show that the scaffold for the Myddosome created by the oligomerisation of $hMyD88^{DD}$ can exist as a preformed structure *in vivo* and suggest an alternate path for Myddosome assembly in which receptor or adaptor TIR engagement with the homologous domain in hMyD88 provides the switch that allows IRAK4 recruitment with the death domain scaffold and further downstream signal transduction.

RESULTS

$hMyD88^{DD}$ spontaneously assembles into helical oligomers

Solutions of $hMyD88^{DD}$ form oligomers at concentrations above 23 μM (Motshwene, et al., 2009). Circular dichroism spectra, in the far-UV, performed on samples of $hMyD88^{DD}$ at concentrations of 35 μM and higher displayed characteristic bands at 209 nm and 223 nm (Figure S1A) which is indicative of α-helical secondary structure. Monomeric $hMyD88^{DD}$ is predominantly helical (Lin, et al., 2010), and this implies that its oligomeric form is also helical and is unlikely to be comprised of denatured aggregates. To obtain hydrodynamic data on the nature of the self-associating $hMyD88^{DD}$ oligomer, sedimentation velocity and sedimentation equilibrium data were acquired on samples having concentrations of 35 μM or higher.

A c(S) analysis of the sedimentation velocity data suggests that the hMyD88^{DD} oligomer is heterogeneous having sedimentation coefficients ranging from approximately 23–34 S (Figure 1A). There is evidence of monomeric hMyD88^{DD} which sediments at 1.5–2 S (Motshwene, et al., 2009) suggesting a dynamic equilibrium between monomeric and oligomeric forms of hMyD88^{DD}.

The frictional coefficient from this analysis was 1.3 but the very flat error surface for this parameter suggests it was not well determined and hence, information regarding the shape or molecular weights from the sedimentation velocity data would be unreliable. The molecular weight recovered from a global analysis of the sedimentation equilibrium data (Figure 1B) collected at two rotor speeds (3200 and 4200 r.p.m.) and two wavelengths (250 nm and 280 nm) was 5.2 MDa. Given the heterogeneous sedimentation velocity data, this likely represents an average molecular weight value. Additionally, because the molar mass of the hMyD88^{DD} monomer is 17.5 kDa, the equilibrium data implies that the helical oligomer is composed of at least several hundred hMyD88^{DD} monomers. The thermal stability of the hMyD88^{DD} helical oligomer was determined by monitoring the fluorescence of SPYRO orange and also by changes in secondary structure at fixed wavelength using circular dichroism spectroscopy both as a function of temperature. Although the measured signal in these methods arise from different sources, the mid-points of the melting profiles are similar corresponding to T_m values of 53.5 °C and 55.7 °C for the fluorescence and CD measurements respectively (Figure S1C,B). Additionally, the pre-transition slope obtained by monitoring the secondary structure content at fixed wavelength suggests that the hMyD88^{DD} helical oligomer likely dissociates before the melting of the helices in the monomeric protein occur.

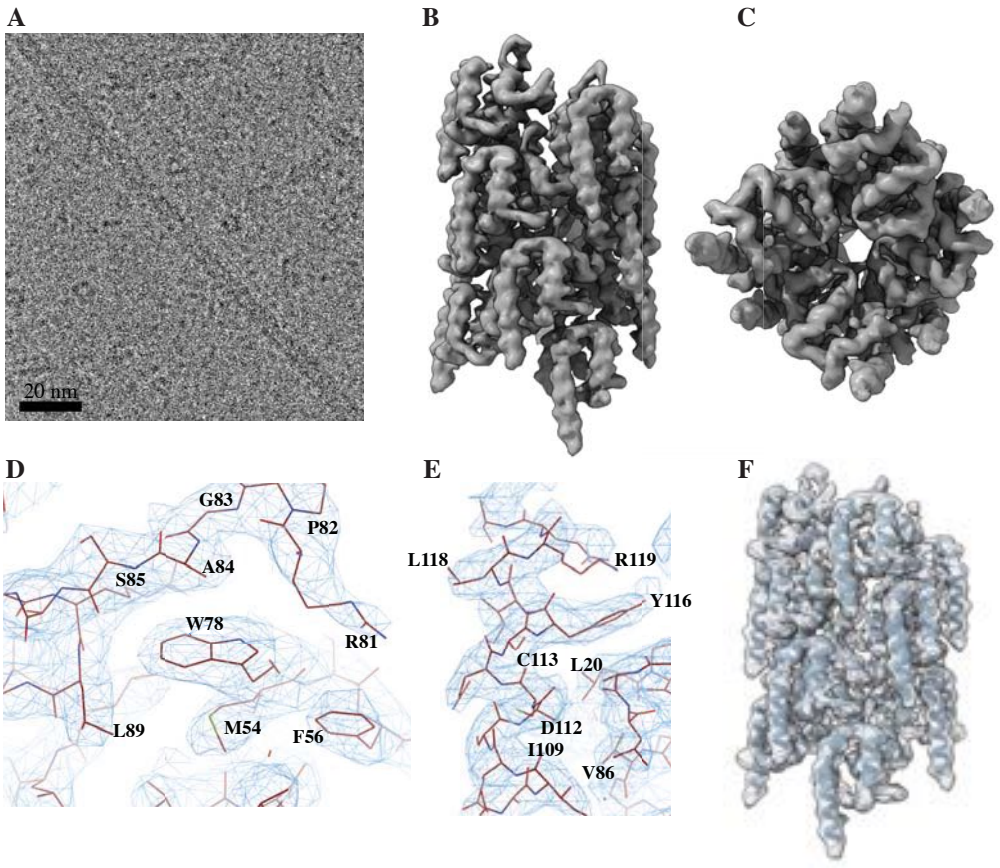

Figure 2 Cryo-EM structure of the hMyD88^{DD} filament at 3.1 Å resolution. (**A**) Typical cryo-EM image of the hMyD88^{DD} filaments which have lengths ranging from approximately 10–1000 nm. (**B–C**) Two views of the reconstructed hMyD88^{DD} complex with the latter looking down the helical axis and showing the approximately 16 Å cavity that spans the filament. The long helix (H6) at the C-terminus of the hMyD88^{DD} is clearly visible. The quality of the cryo-EM map allowed unambiguous fitting of atomic models of hMyD88^{DD} monomers into the reconstructed map. Typical side chain densities of some resides in the hydrophobic region surrounding W78 **(D)** and the sixth α-helix, H6, (**E**). Cartoon representation of a thirteen subunit segment of the hMyD88^{DD} monomers superimposed onto the reconstructed cryo-EM map (**F**).

Cryo-EM structure of the hMyD88^{DD} helical filament

Having established that hMyD88^{DD} can self-associate into helical assemblies, we sought to determine the precise arrangement of these oligomeric forms. Preliminary negative stain electron microscopy revealed

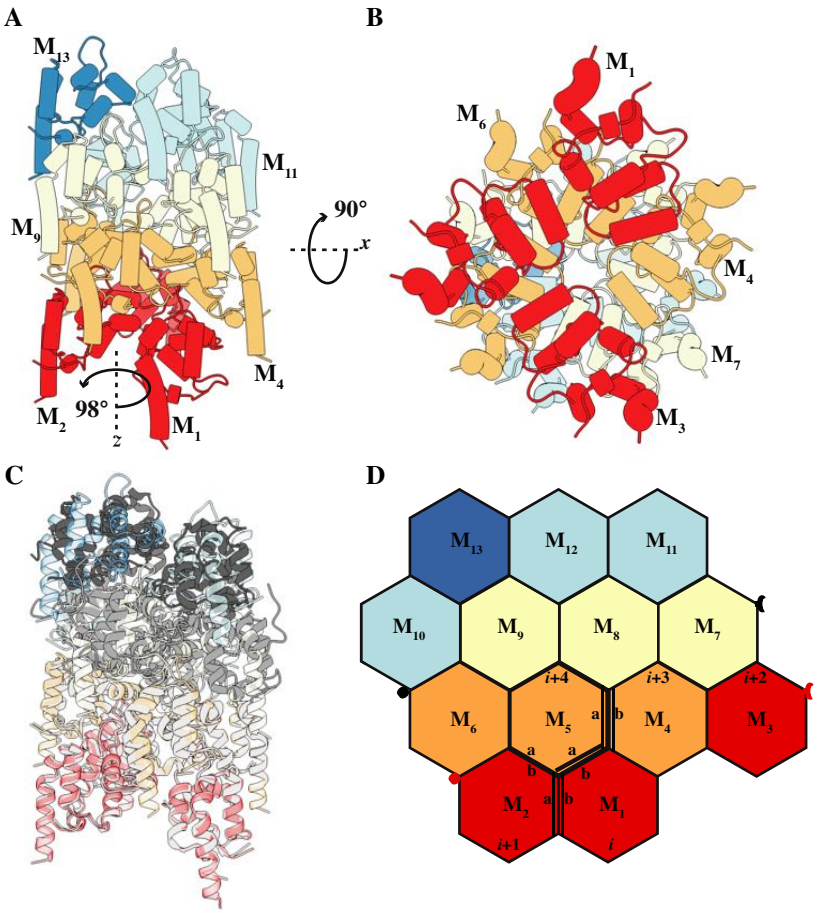

Figure 3 Structure of the hMyD88^{DD} filament. (**A**) A segment comprised of thirteen hMyD88^{DD} subunits (M1–M13). The thirteen death-domain subunits are assembled in layers and each layer is coloured differently. (**B**) View along the helical axis of the hMyD88^{DD} filament and some inter-subunit contacts. (**C**) Superposition of the heterotrimeric hMyD88^{DD} (light-grey) IRAK4^{DD} (medium-grey) and IRAK2^{DD} (dark-grey) Myddosome onto the hMyD88^{DD} filament. The MyD88 layer of the heterotrimer superimposes onto the helical filament with an r.m.s.d. of 0.76 Å. (**D**) Representation of the different interfaces present in the hMyD88^{DD} helical filament. The interaction between the $i + 1$ and $i + 4$ subunits generates a Type I interface while that between the i and $i + 4$ subunits generates a Type II interface. The Type III interface which occurs at the intersection of Type I and II interfaces is represented by the interaction between the $i + 3$ and $i + 4$ subunits. Red and black clasps indicate where the M_3 and M_7 subunits fit when the two-dimensional hexagons are wrapped to represent the helical filament.

that hMyD88^{DD} assembled into filaments of varying lengths, with a diameter of approximately 68 Å and these were corroborated by cryo-EM images (Figure 2A). Subsequent analysis of the cryo-EM data using SPHIRE (Moriya, et al., 2017) revealed that the filaments possessed helical symmetry having an axial rise of approximately 6.2 Å and an azimuthal rotation angle of 98.2°. Iterative helical real-space refinement (Egelman, 2000) as implemented in RELION (He, et al., 2017; Scheres, 2012) was used to calculate a 3.1 Å cryo-EM map—as judged by the FSC = 0.143 criterion (Figure S3C)—of the hMyD88^{DD} filament with refined helical parameters of 5.98 Å and 98.01°. The computed maps were of excellent quality with elements of secondary structure clearly visible (Figure 2B–C). A copy of the hMyD88^{DD} monomer derived from the atomic coordinates of the hetero-trimeric MyD88-IRAK4-IRAK2 death domain complex (Lin, et al., 2010) was fitted into the map using MOLREP (Vagin, et al., 2001) and the atomic coordinates refined using PHENIX (Adams, et al., 2010). Typical fits of the refined side-chain density into the post-processed EM-map are shown (Figure 2D–E) which clearly illustrate the good agreement between map and model. This enabled model building to extend the N-terminus by a single residue and also the C-terminal helix (H6) by three residues relative to the previously deposited model (Lin, et al., 2010) and, consequently, extends the death domain boundary of hMyD88 to Q121. The r.m.s.d. between a MyD88^{DD} subunit taken from the filament and that from the crystal structure of the Myddosome (Lin, et al., 2010) was 0.76 Å. Figure 2F shows the refined coordinates of thirteen hMyD88^{DD} subunits superimposed on the cryo-EM map. The tower-shaped layered structure is reminiscent of the ternary hMyD88-IRAK4-IRAK2 complex (Lin, et al., 2010). Interestingly, although the

hMyD88^{DD} construct used has a thirty residue segment belonging to the intermediate domain (ID) which links the death and TIR domains, this region is absent from the reconstructed maps suggesting that it lacks ordered secondary structure. This suggests that one role of the intermediate domain is to act as a flexible tether which allows the TIR and death domains of hMyD88 to adopt a range of orientations with respect to each other. In addition, it implies that the ID plays no role in the self-association of hMyD88^{DD}. Parameters relating to cryo-EM data collection, refinement and validation are summarised in Table 1.

Table 1 Cryo-EM data collection, refinement and validation statistics for the hMyD88^{DD} helical filament.

	hMyD88^{DD}
Data Collection	
Microscope	Titan Krios
Camera	Falcon III
Operating voltage (kV)	300
Magnification	$75,000 \pm 1,500$
Dose per frame (e/Å^2)	0.92
Pixel size (Å)	1.06
Defocus (μm)	-0.9 to -3.2
Reconstruction	
Overlapping helical segments	1,229,488
Point group symmetry	C_1
Refined helical symmetry	5.98 Å; 98.01°
Resolution (Å)	3.1
Resolution measure	Map FSC
Map sharpening B-factor (Å^2)	-150
Model composition	
Monomer (protein residues; non-hydrogen atoms)	103; 2,206
13-mer (protein residues; non-hydrogen atoms)	1,339; 10,660
Refinement and Validation (monomer, 13-mer)	
R.m.s bond length (Å)	0.005; 0.007
R.m.s angles (°)	0.94; 1.041
Rotamer outliers (%)	0; 0
Ramachandran favoured (%)	95.05; 92.08
Ramachandran allowed	4.95; 7.92
Molprobity score	1.44; 1.64
Clashscore	3.02; 3.63

Intersubunit interactions stabilise filament formation

The hMyD88^{DD} filament can be described as a single-stranded left handed helix of death domains and is similar to the ternary death domain complex (Lin, et al., 2010). However, unlike the arrangement in the hMyD88-IRAK4-IRAK2 death domain complex, each hMyD88^{DD} subunit—with the exception of those at the end of the filaments—resides in an equivalent environment. The architecture of the helical death domain filament is shown in Figure 3A using a thirteen subunit segment. Each individual hMyD88^{DD} monomer makes immediate contact with six neighbouring death domains and this is most clearly seen in Figure 3D where the three dimensional filament is represented in two-dimensions. The inter-subunit interfaces are comprised of Type I(a/b), Type II(a/b) and Type III(a/b) interactions (Park, et al., 2007; Weber, et al., 2001) (see Figure S4). The Type I interface is predominantly electrostatic in nature and involves interactions between H1 and H4 on one subunit (Type Ia) with H2 and H3 of a second subunit. The residues involved in the Type I(a/b) interface of the hMyD88^{DD} filament which is represented by the M_2 —M_5 interaction ($i+2$ and $i+4$ subunits) (Figure 3C) bury 622 Å^2. The Type II interface, which occurs between the i and $i+4$ subunits, for example, is smaller than the Type I interface and buries 511 Å^2. This surface involves the interaction between residues on H4 and the loop connecting the H4 and H5 helices on one subunit (Type IIa) with residues on H6 and

the H5-H6 loop on a second subunit (Type IIb). The Type III interface involves interaction between residues on H3 of one subunit (Type IIIa) and residues close to the H1–H2 and H3–H4 loops of the second subunit. This surface is typified by the $i + 3$ and $i + 4$ interaction (Figure 3C) and is the smallest surface burying only 253 Å^2. As illustrated in Figure 3D, Type I and Type II interactions occur between successive layers while the Type III interaction occurs within each layer. Therefore hMyD88^{DD} filament formation likely proceeds via an initial 'seed' consisting of a Type I or Type II homodimer which then associates into a tetramer and continues to grow. Details of the residues involved in the various interfaces are listed in Table S1. Superposition of the ternary MyD88-IRAK4-IRAK2 death domain structure on that of the hMyD88^{DD} filament is shown in Figure 3C. The r.m.s.d. between MyD88^{DD} from the ternary complex and that from filament is 0.76 Å confirming the similarity in architecture of both structures. The largest differences occur between the loops connecting the H1–H2, H3–H4 and H4–H5 helices (Figure S5).

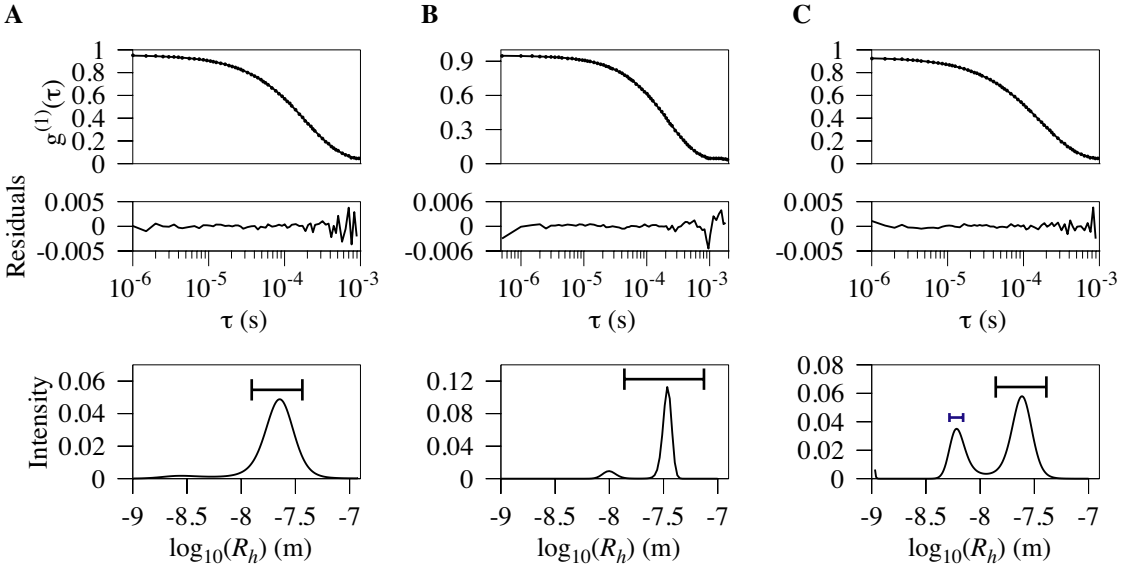

Figure 4 IRAK4^{DD} associates with the hMyD88^{DD} filament. The upper and middle panels show plots of the autocorrelation as a function of time and residuals after fitting while the bottom panel shows a plot of intensity as a function of hydrodynamic radius for the hMyD88^{DD} death domain filament at 34 μM (**A**) and 45 μM (**B**) with the length of each bar representing the average filament length. At the highest concentration, the complex has a hydrodynamic radius of approximately 31 ± 9 nm and the distribution shifts to larger oligomers. The addition of IRAK4^{DD} death domain (**C**) results in the formation of the previously characterised hMyD88^{DD}-IRAK4^{DD} Myddosome (blue).

IRAK4^{DD} interacts with the hMyD88^{DD} filament

A common view of the TLR signal transduction pathway envisages receptor dimerisation as the crucial step that facilitates association of TIR domains on both the receptor and the adaptor MyD88. MyD88, subsequently recruits the IRAKs to complete the signalling platform. Given that IRAK4 is indispensable for MyD88 dependent signalling (Suzuki, et al., 2002), we sought to determine if the helical hMyD88^{DD} filament interacts with the death domain of IRAK4. Dynamic light scattering was used to measure the size distributions of the hMyD88^{DD} filament at two concentrations and additionally, when titrating aliquots of IRAK4^{DD} such that the effective concentration of hMyD88^{DD} was always above that required for filament formation. Because IRAK4^{DD} is monomeric, a change in the size distribution from the hMyD88^{DD} filament to the 6–8:4 hMyD88^{DD} -IRAK4^{DD} Myddosome should be observable. Figure 4A–B, shows DLS measurement of hMyD88^{DD} filaments at 34 μM and 45 μM. At 45 μM, the hMyD88^{DD} oligomers are longer as would be expected from a process in which filament growth is concentration dependent. The addition of aliquots of IRAK4^{DD} to the hMyD88^{DD} oligomer in Figure 4B enables the formation of the 6:4 hMyD88^{DD}-IRAK4^{DD} Myddosome (Figure 4C). This was confirmed by DLS measurements using purified samples of the hMyD88^{DD}-IRAK4^{DD} Myddosome (Figure S2B) in addition to sedimentation velocity experiments (Figure S2A) which recovered a sedimentation coefficient value of 6.1 S which is similar to the published value (Motshwene, et al., 2009). Of note, there is no evidence of small oligomeric species, for example, a heterodimer of hMyD88^{DD} and IRAK4^{DD}. Consequently, a mechanism of Myddosome assembly which involves the stepwise dissociation of hMyD88^{DD} monomers from the filament by IRAK4^{DD} and their reconstitution into a 6:4 hMyD88^{DD}-IRAK4^{DD} complex is not supported. In contrast, the data supports a model in which IRAK4^{DD} monomers associate with one end of the helical filament resulting in the formation of a transient 4-IRAK4^{DD}-hMyD88^{DD}-filament and its

subsequent dissociation to produce the 6:4 hMyD88^{DD}-IRAK4^{DD} Myddosome and a shortened hMyD88^{DD} filament (Figure 4C).

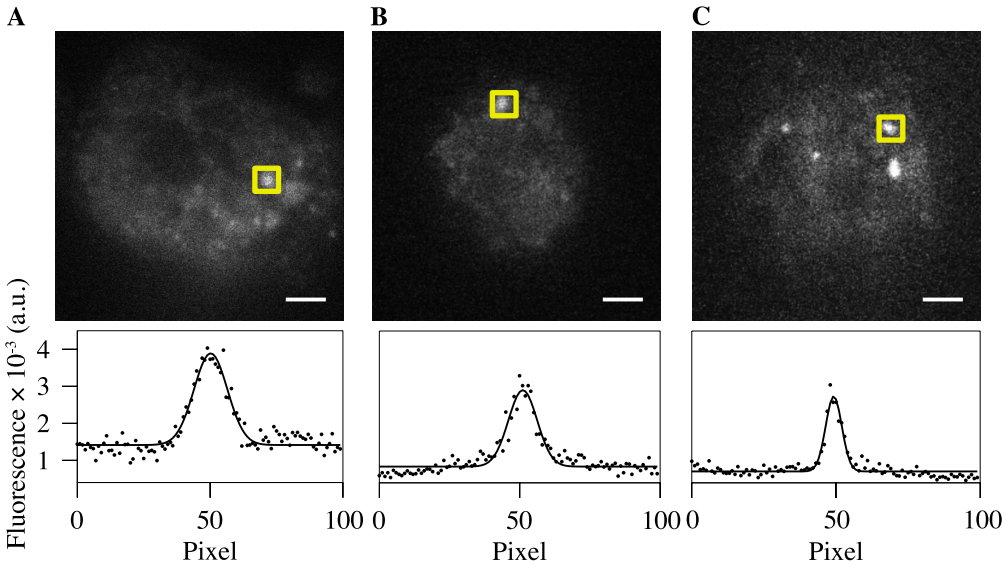

Figure 5 Full-length MyD88 self-associates to produce a pre-Myddosome scaffold *in vivo*. Representative TIRFM (**A**) and Light-sheet (**B**) images of GFP-MyD88 expression in unstimulated virally transduced MyD88$^{-/-}$ bone derived macrophage ($n = 31$). Panel (**C**) shows a typical TIRFM image after stimulation with LPS ($n = 8$). Fitting the intensity distribution of the oligomeric GFP-MyD88 species using a box size of 100-pixels to a Gaussian allows determination of the peak intensity which is used along with that of monomeric GFP-MyD88 (Figure S6C) to estimate the number of associating MyD88 monomers. For TIRFM and Light Sheet illumination in both unstimulated and LPS stimulated cells, the estimated number of MyD88 monomers was 1 and 5 ± 1 respectively. The length of the scale bar is 5 μm.

The Myddosome scaffold is preformed *in vivo*

Overexpression of MyD88 in several cell types results in large cytosolic aggregates of unknown structure and composition (Jaunin, et al., 1998; Nishiya, et al., 2007). Additionally, using a cell-free expression system that enabled the tuning of protein expression levels, it has been shown that MyD88 polymerises at low concentrations by a process in which both death and TIR domains are implicated (O'Carroll, et al., 2018). Given that hMyD88^{DD} self-associates into helical filaments *in vitro* having identical symmetry to that of the hMyD88^{DD}-IRAK4^{DD}-IRAK2^{DD} Myddosome (Lin, et al., 2010), we sought to determine whether MyD88 oligomerisation *in vivo* could produce a cytosolic 'pre-Myddosome' scaffold prior to receptor activation. In a previous study (Latty, et al., 2018), we used immortalised bone marrow derived macrophages from MyD88$^{-/-}$ mice that had been reconstituted with a functional, fluorescent form of MyD88 to study Myddosome formation. This experimental system accurately recapitulates the physiological signalling process as stimulation with LPS leads to rapid formation of Myddosomes at the plasma membrane and NFkB activation. We have therefore used both TIRFM and single molecule Light-Sheet imaging to estimate the stoichiometry of MyD88 in unstimulated and LPS treated cells.

Figure 5 shows TIRFM and LSFM images of GFP-MyD88 expression in unstimulated cells (**a** and **b**) and the corresponding TIRFM (**c**) image of cells stimulated with LPS. Analysis of the intensity distribution (Figure S6A,B) in unstimulated cells by both methods (Ponjavic, et al., 2018) reveals the presence of monomeric, dimeric and hexameric populations of GFP-MyD88. The average number of preformed hexamers obtained using LSFM from thirty-one unstimulated cells was 1 while cells stimulated with LPS, typically contained 3–4 MyD88 hexamers in a given imaging volume. Given that signalling is not observed in unstimulated cells (Latty, et al., 2018), these data imply that unstimulated cells contain a small population of hexameric MyD88 oligomers whose conformation does not allow recruitment of IRAKs.

DISCUSSION

Activation of TLRs initiates a signalling cascade that culminates in the production of pro-inflamatory molecules. The commonly accepted view holds that the initial event involves ligand binding to LRR motifs on the receptor ectodomain. This creates activated homo- or hetero-dimeric receptor complexes whose cytosolic TIR domains engage with other TIR containing adaptor proteins including hMyD88 and the subsequent formation of the Myddosome (Lin, et al., 2010; Motshwene, et al., 2009) which constitutes the core of the

bow-tie (Beutler, 2004; Friedlander, et al., 2015) signaling network for all TLRs except TLR3. While interactions between the TIR domains of TLR's and adaptors and also TIR containing adaptors has long been implicated, direct evidence *in vitro* has been sparse. However, recently, the TIR domain of MAL/TIRAP was found to form open-ended homo-oligomeric helical filaments and, additionally, hetero-oligomeric filaments with the homologous domain of hMyD88 via a two stranded head-to-tail arrangement (Ve, et al., 2017). Assembly of the MAL^{TIR} filament involves intra- and inter-strand interactions and this has led to a model of TLR signalling in which receptor dimerisation on ligand binding leads to intrastrand contacts between receptor TIR domains. Subsequent interstrand interaction between the newly created receptor TIR dimer interface with other TIR containing adaptors such as MAL^{TIR} or $hMyD88^{TIR}$ then occurs leading to the formation of higher order receptor associated complexes (Ve, et al., 2017).

The above suggests a stepwise, sequential mechanism for the assembly of receptor and adaptor TIRs and, by extension, the Myddosome. Additionally, it implies that oligomerisation of hMyD88 is driven, at least in part, by receptor TIR-$hMyD88^{TIR}$ or MAL^{TIR}-$hMyD88^{TIR}$ interactions. However, our finding that $hMyD88^{DD}$ spontaneously forms helical filaments whose architecture is identical to that observed in the heterotrimeric hMyD88-IRAK4-IRAK2 death domain complex (Lin, et al., 2010) suggests that the helical arrangement adopted by hMyD88 during signalling is an intrinsic property of its death domain and is therefore independent of its interaction with either receptor or adaptor TIRs. Given that these filaments also interact with $IRAK4^{DD}$ to form the previously characterised $hMyD88^{DD}$-$IRAK4^{DD}$ complex (Motshwene, et al., 2009), it also implies that the $hMyD88^{DD}$ scaffold may not assemble sequentially during signalling but may exist, intracellularly, as a preformed structure. Overexpression of full-length MyD88 in HEK293T, bone marrow-derived macrophages or HeLa cells resulted in large species scattered throughout the cytosol having sizes that are in the micron range (Jaunin, et al., 1998; Nishiya, et al., 2007). We contend that these previously uncharacterised forms of hMyD88 are in fact helical filaments assembled from $hMyD88^{DD}$ interactions as described. The physiological role of these filaments is unknown but our finding that MyD88DD alone self-assembles implies that 'super-MyDDosomes' which contain more than six copies of MyD88 are possible and, additionally, prompted us to look for oligomeric forms of MyD88 in unstimulated cells. Given that filament formation and length is concentration dependent, one expects that in cellular contexts where hMyD88 expression is normal, the oligomeric helical forms will attain shorter lengths than those observed when the protein is overexpressed. This is consistent with our finding that hexameric oligomers of full-length hMyD88 exist in unstimulated macrophage cells and with recent reports which suggest that the polymerisation of full-length MyD88 occurs at concentrations in the nM range by a process that requires the death and TIR domains (O'Carroll, et al., 2018).

Models of Myddosome assembly should be consistent with reported signalling data. For example, a truncated hMyD88 construct lacking only the TIR domain elicited NFκ-B activity similar to that of the full length protein (Medzhitov, et al., 1998; Wesche, et al., 1997). This suggests that the death and intermediate domains are sufficient to recruit IRAKs whose subsequent phosphorylation determines signal flux through TRAF6, and hence, NFκ-B production. It also implies that a key step in Myddosome formation, the oligomerisation of hMyD88 death domains, occurs intracellularly without the involvement of the TIR domain of receptor, other adaptors or that of hMyD88 itself. Another interesting observation regards $MyD88_S$, a splice variant which lacks the intermediate domain and inhibits TLR/IL-1R signalling by preventing the recruitment of IRAK4 and hence, IRAK4 mediated phoshorylation of IRAK1 (Burns, et al., 2003). The heterotrimeric Myddosome structure (Lin, et al., 2010) reveals that $IRAK4^{DD}$ interacts with only one end of the helical scaffold created by the oligomerisation of $hMyD88^{DD}$. Thus, the inability of $hMyD88_S$ to associate with IRAK4 could be due to failure of $hMyD88_S^{DD}$ to self-associate in the absence of the intermediate domain or obstruction of the surface required for IRAK4 binding by the TIR domain of $hMyD88_S$. The latter explanation is more plausible because the construct used by Lin and colleagues (Lin, et al., 2010) lacks the intermediate domain but is able to self-oligomerise and associate with $IRAK4^{DD}$. The preceding raises the possibility that the TIR domain of hMyD88 may function as a binary switch during TLR/IL-1R signalling. It has been reported that forced dimers of $MyD88^{TIR}$ interact strongly with activated TLRs (Fekonja, et al., 2012). In the absence of receptor or adaptor TIR engagement with hMyD88, its TIR domain exerts an inhibitory effect thus preventing the recruitment of IRAK4 and subsequent Myddosome formation. Conversely, this inhibition is removed when either activated receptor TIR domains engage directly or indirectly via MAL with the TIR domain of hMyD88. Removal of inhibition by the TIR domain of hMyD88 is facilitated by the intermediate domain which is envisaged to act as a 'lever' allowing the TIR domain of hMyD88 to adopt an orientation in which it no longer blocks the surface on the $hMyD88^{DD}$ scaffold required for $IRAK4^{DD}$ engagement and, additionally, positions the TIR domain optimally for interaction with the juxtamembrane TIR domains of the activated receptor or

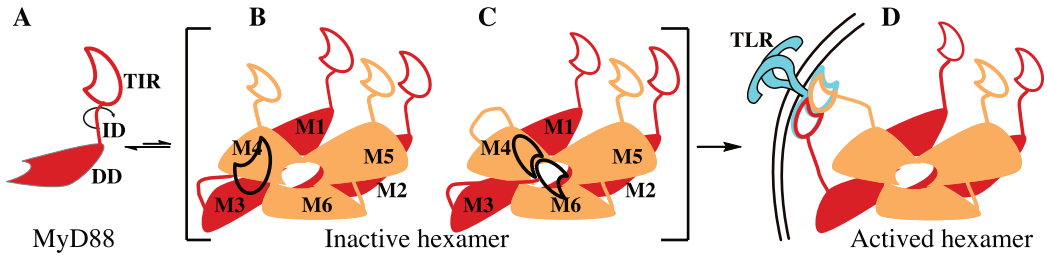

Figure 6 Model of TLR signalling in which the TIR domain of hMyD88 acts as a binary switch. (**A**) MyD88 contains an N-terminal death domain (DD) and a C-terminal TIR domain which are linked by an intermediate domain (ID) that is devoid of ordered secondary structure. Cytosolic MyD88 reversibly self-associates via its DD to form an inactive two-layered (M1–M3 and M4–M6) hexameric scaffold that is incapable of producing a signalling MyDDosome because the M3–M6 surface which is required for IRAK4 DD interaction is obscured by the TIR domain. This inactive conformation could be caused either by the TIR domain of the M3 MyD88 subunit (black) from the first layer blocking the M4 and M6 IRAK4 interaction surfaces (**B**) or, alternatively, weak association between the M3 and M4 TIR domains, for example (**C**). Microbe associated molecular pattern and co-receptor binding—where required—to the TLR receptor ectodomain enable receptor dimerisation and activation of receptor TIR domains which associate directly via intra-strand contacts (**D**). This receptor TIR dimer interacts strongly with the hMyD88 TIR domains via interstrand contacts directly or via MAL/TIRAP and this relieves the inhibition of the TIR domain and allows recruitment of IRAK4 and IRAK2 onto the hMyD88 scaffold where signal transduction proceeds by phosphorylation.

adaptor TIRs. The above leads to a second model of TLR signalling which is summarised in Figure 6. Intracellularly, monomeric hMyD88 exists in equilibrium with low concentrations of short hexameric helical forms which have the same architecture as the Myddosome. However, the TIR domain prevents constitutive pathway activation by obscuring the surface on the MyD88 platform to which IRAK4 interacts. Receptor activation on MAMP binding creates the necessary intrastrand receptor dimer as proposed (Ve, et al., 2017) and this newly created surface recruits the hMyD88 assembly by homotypic TIR-TIR interactions which then allows recruitment of the IRAKs to the hMyD88 scaffold. In this model, the hexameric MyD88 platform is envisaged to act as a 'sentinel' that can be quickly utilised. Subsequent signalling may then proceed via nucleation as previously described (Gay, et al., 2014). Interestingly, a constitutively active mutant of hMyD88, L265P, which has been implicated in several cancers including Waldenström's macroglobulinemia (Ngo, et al., 2011; Treon, et al., 2012) does not require receptor attachment for signalling (Avbelj, et al., 2014). Although the L265P mutation maps to the intrastrand TIR interface (Lin, et al., 2010) the non requirement for receptor TIR engagement for NFκB production strongly suggests that this mutation is involved in a process that relieves the inhibition of the TIR domain as described.

TLRs respond to a range of ligand concentrations and this bears resemblance to processes occurring in chemotatic bacteria whose receptors simultaneously detect low concentrations and ligand gradients over several orders of magnitude (Mesibov, et al., 1973). A mathematical model suggests that this requirement can be satisfied if both single receptors and clusters of receptors reside on the cell (Bray, et al., 1998). Receptor clustering has been observed in TLR4 signalling (Motshwene, et al., 2009) and it is likely that other TLRs behave similarly. Additionally, during TLR signalling it is unlikely that only a specific receptor type is activated given that pathogens will produce a variety of activating ligands. It has been shown that TLR pathway cross-talk enhances cytokine secretion (Lin, et al., 2017) and so different TLR types localised in the same compartment—for example, plasma membrane bound TLR4 and TLR1/2 which respond to bacterial lipopolysaccharide and lipopeptide—could act synergistically. Whether the TIR domains of hMyD88 from one Myddosome are able to simultaneously interact with the receptor TIR dimer or the MAL-TIR/receptor TIR tetramer from two different TLR receptor types, while plausible, is currently not known.

In summary, this study proposes an additional model for TLR signalling via the Myddosome in which oligomerisation of hMyD88 to produce the scaffold required for IRAK4 interaction is produced prior to receptor activation. Constitutive pathway activation is, however, prevented by the TIR domain of hMyD88 which is inhibitory until TIR dimers from this scaffold engage with activated receptor TIR dimers or receptor TIR/MAL TIR heterotetramers.

Author Contributions

M.C.M. conceived, designed, performed experiments and analysis and wrote the manuscript. D.B. helped with calculations in RELION. P.A.P. contributed to indexing using SPHIRE, and provided general guidance on cryoEM methods. B.L. performed TIRFM and LSFM data collection and analysis. L.H. provided iBMDM's

transduced with TLR4 and GFP-MyD88. C.E.B. and D.K. provided resources and N.J.G. helped with original conception.

Acknowledgements

This work was funded by a Wellcome Trust investigator award WT100321/z/12/Z to N.J.G. P.A.P is supported by the National Institutes of Health R01 GM60635 and P01 GM 121203. D.K. is supported by a Royal Society Research Professorship (RP150066) and C.E.B. by a Wellcome Trust investigator award 108045/Z/15/Z. We thank Dr. Dimitri Y. Chirgadze for assistance with data collection at the Cryo-EM Facility, Department of Biochemistry, University of Cambridge which is funded by grants from the Wellcome Trust (206171/Z/17/Z, 202905/Z/16/Z), the Departments of Biochemistry and Chemistry, the Schools of Biological Sciences and Clinical Medicine and the University of Cambridge. Finally, thanks to Doug Golenbock and Kate Fitzgerald (University of Massachusetts Medical School) for the MyD88$^{-/-}$ and TLR4$^{-/-}$ iBMDM cells.

Cryo-EM maps and atomic coordinates are deposited in the Electron Microscopy Data Bank (EMD-4405) and Protein Data Bank (PDB 613N) respectively.

STAR METHODS

LEAD CONTCT AND MATERIALS AVAILABILITY

Further information and requests for resources and reagents should be directed to, and will be fulfilled by, the lead contact Martin C Moncrieffe (mcm35@cam.ac.uk). This study did not generate new unique reagents.

EXPERIMENTAL MODEL AND SUBJECT DETAILS

Bacterial Strains

Escherichia coli BL21DE3 Rosetta 2 cells (Novagen) used for protein production were cultured in LB medium supplemented with the appropriate antibiotics.

Human HEK293T Cells

HEK293T cells were culfured in DMEM (Gibco) supplemented with 10% FCS and 100 U/ml penicillin and 100 µg/ml streptomycin.

METHOD DETAILS

Protein expression and purification

The expression and purification of IRAK4^{DD} has been described previously (Motshwene, et al., 2009). The N-terminal death and intermediate domains of hMyD88 (1–151) in addition to a non-cleavable C-terminal Streptactin II tag were cloned into pMCSG7 (DNASU) and expressed as an N-terminal hexahistidine-tagged fusion protein in *E. coli* BL21DE3 Rosetta 2 (Novagen). Cells were grown in LB medium with shaking (220 rev/min) at 310 K to an OD_{600nm} of 0.8 after which the temperature was reduced to 293 K and 1 mM IPTG added and protein expression continued for for 12–16 hrs. Cells expressing hMyD88^{DD} were resuspended in Buffer A (20 mM Tris, 30 mM NaCl, 1 mM EDTA) supplemented with 1 ml BugBuster (Novagen) pH 8.0 and lysed using an Emulsiflex C5 (Avestin) homogeniser. The lysate was clarified by centrifugation at 99000 × *g* for 20 min at 277 K, applied to a 5 ml StrepTrap HP column (GE Healthcare), washed with ten column volumes of Buffer A. The bound protein was eluted with 10 mM desthiobiotin (Sigma) in Buffer A. Pooled samples containing hMyD88^{DD} were incubated with TEV protease at 277 K to remove the hexahistidine tag, concentrated and further purified by S200 (GE Healthcare) size exclusion chromatography using a buffer containing 20 mM Tris, 20 mM NaCl, pH 8.0 and 5% glycerol for the AUC samples.

Circular dichroism spectroscopy and differential scanning fluorometry

Spectra in the far-UV (195–250 nm) were recorded on an Aviv 410 spectropolarimeter. Protein samples (35 µM) were in 20 mM Tris, 20 mM NaCl, 5% glycerol pH 7.5. The instrument bandwidth was 1 nm, the wavelength scan increment 0.5 nm and the averaging time 1 s. Three spectra were accumulated and averaged. Continuous temperature scans at fixed wavelength (222 nm) were performed in the range 283—368 K with a temperature step of 1 K. Differential scanning fluorometry experiments were performed using Spyro Orange (Thermo Fisher) as the fluorescent probe and a Rotor-Gene 6000 (Qiagen) thermocycler.

Analytical ultracentrifugation

Analytical sedimentation velocity and equilibrium measurements were performed using a Beckman XL-A ultracentrifuge at 293 K and a sample concentration of 35 µM. For sedimentation velocity measurements, the sample and reference volumes were both 400 µl and data were acquired at 120 s intervals at rotor speeds of 30,000 rev/min using an An60Ti rotor (Beckman Coulter). Buffer density and viscosity were estimated using SEDINTERP (Laue, et al., 1992) and the sedimentation profiles were analysed with SEDFIT (Schuck, 2000). Sedimentation equilibrium experiments were conducted using 180 µl sample volume. Absorbance data was acquired at 250 and 280 nm and rotor speeds of 3200 and 4200 rev/min. The attainment of equilibrium was

determined by subtraction of successive scans until the root mean square difference was constant. Global analysis of the equilibrium data was performed using SEDPHAT (Schuck, 2003).

Cryo-EM reconstruction of the hMyD88^{DD} helical filament

A 4 µl sample of hMyD88^{DD} at 1 mg/ml was applied to a glow discharged Quantifoil R1.2/1.3 holey carbon grid (Quantifoil). Grids were blotted and frozen in liquid ethane using a Vitrobot Mark IV (FEI) instrument (277 K, blot force 0, blot time 3 s, humidity 100%) and stored in liquid nitrogen. Grids containing vitrified samples were imaged using a Titan Krios (FEI) microscope operating at 300 kV and with a Falcon III (FEI) direct electron detector in counting mode. Movies were recorded using a nominal magnification of $75,000 \pm 1500\times$ and a calibrated pixel size of 1.06 Å/pixel. During data collection, 48 frames were acquired with a total dose of 44.1 e·Å^{-2} corresponding to a per frame dose of 0.92 e·Å^{-2}. An initial estimate of the helical symmetry was obtained using SPHIRE (Moriya, et al., 2017). Filaments were selected from 200 micrographs using *sxhelixboxer.py* and segments were windowed using a box size of 220 × 220 pixels with 10 pixels overlap between them. The averaged power spectrum of all aligned patches was then calculated which revealed a pattern of layer lines typical of objects with helical symmetry (Figure S3) having a meridional reflection at 0.161 Å^{-1} implying that the axial rise per subunit is approximately 6.2 Å. The azimuthal rotation per subunit obtained by indexing was 98.2°. Subsequent calculations were performed in RELION-3.0 (Scheres, 2012). Movie stacks were motion corrected using MotionCor2 (Zheng, et al., 2017) and contrast transfer function parameters were estimated with Gctf-1.06 (Zhang, 2016) using an amplitude contrast of 0.1. Micrographs that had large defocus values relative to the nominal values set at the microscope were not used in subsequent processing. The range of defocus values use d was −0.9 µm to −3.2 µm. Parameters for auto-picking filaments in RELION were optimised using twenty-five micrographs having defocus values from the range given above. Segments were extracted using a box size of 220 pixels and an overlap of 7 pixels yielding 1,257,342 overlapping helical segments from all micrographs. Reference-free 2D classification using a regularisation value of $T = 2$ was then performed to identify homogeneous subsets. The selected class averages contained 1,229,488 overlapping helical segments. An initial model was generated using the Stochastic Gradient Descent algorithm (Punjani, et al., 2017) as implemented in RELION. High resolution refinement using all 1,229,488 overlapping segments was performed during which the helical parameters were refined using 3D auto-refinement in RELION. The refined helical symmetry values were 5.98 Å (rise) and 98.01° (azimuthal rotation per subunit). A resolution estimate of 3.1 Å was obtained using the Fourier shell correlation at 0.143 between two independently refined half-maps. The map was sharpened using the post-processing routines in RELION and a soft mask (Figure S3E) resulting in a *B*-factor of −150 Å^2. MOLREP (Vagin, et al., 2001) was used to place a single copy of the hMyD88^{DD} monomer taken from the crystal structure of the hetero-oligomeric hMyD88^{DD}-IRAK4^{DD}-IRAK2^{DD} complex (PDB code, 3MOP) (Lin, et al., 2010) into the post-processed cryo-EM map. Several rounds of real space refinement in PHENIX (Adams, et al., 2010; Wang, et al., 2014) followed by model building in COOT (Emsley, et al., 2010) were then performed. MOLREP (Vagin, et al., 2001) was then used to place thirteen copies of the extended hMyD88^{DD} model into the density followed by real space refinement as before. A comparison of the reconstructed map and the PDB model in Chimera(Pettersen, et al., 2004) reveals that the pixel size at the specimen level was 1.065 Å/pixel (Figure S3D). Model validation was performed using PHENIX (Adams, et al., 2010). Figures containing Cryo-EM maps and PDB models were made using UCSF ChimeraX (Goddard, et al., 2018)

Dynamic light scattering

DLS measurements were performed at 298 K using a Zetasizer Nano S (Malvern Panalytical) instrument and a Hellma quartz cuvette with a 3 mm path length and centre 9.65 mm. All protein samples were passed through 20 µm filters prior to use. 20 µl of MyD88^{DD} (45 µM) was placed into the cuvette and aliquots of 0.8 mM IRAK4^{DD} added so that the total volume in the cuvette did not exceed 26 µl. All measurements were performed at 298 K and analysed using the continuous hydrodynamic radius distribution model in SEDFIT (Schuck, 2000).

Cell culture

The generation of murine immortalised bone marrow derived macrophage (iBMDM) cells expressing GFP-MyD88 from MyD88$^{-/-}$ iBMDMs has been described (Latty, et al., 2018). HEK293T cells were seeded at approximately 50% confluency into 12-well plates, transfected using a 3:1 (µl:µg) ratio of Genejuice (Novagen) transfection reagent and incubated for 96 h at 310 K and 5% CO_2. A total of 1.5 µg of plasmid DNA (0.5 µg each of p891, pMDG and pHR MyD88GFP) was used per well. The supernatant containing lentiviral particles was centrifuged for 5 min at 1200 rev/min, diluted (1:64) using complete DMEM medium and added to MyD88-/- iBMDMs for 24 h at 310 K and 5% CO_2. The medium was then replaced with complete DMEM and iBMDMs grown for an additional 24 h.

Microscopy

Details of the experimental procedures used for acquiring TIRFM and LSFM images have been published (Ponjavic, et al., 2018). A 15 mW fibre-coupled 488 nm diode laser (iFLEX-2000, Qioptic) and an excitation filter (FF01- 488/6-25, Semrock) was used. Light enters the microscope (Eclipse Ti-U, Nikon) through a 100×, 1.49 numerical aperture (NA) oil immersion objective lens (MRD01991, Nikon) and is focused at the back focal plane of the objective lens. The internal magnification of the microscope was used to achieve a final magnification of 150×. The fluorescence emission was bandpass filtered (67-031, Edmund Optics) and focused on to an EMCCD camera (Evolve 512 Delta, Photometrics). Coverslips were plasma cleaned (Harrick Plasma) in an Argon atmosphere for 30 min and coated with solutions of 0.01% (w/v) poly-L-lysine 150-300 kDa (Sigma-Aldrich). The coated coverslips were then washed three times in PBS. 40 µl aliquot of cells (25000 cells/ml) was added to the coated coverslips and stimulated when required by the addition of 2 µl of 100 ng/ml LPS. Two cylindrical lens were used to generate a wide sheet of light and a perpendicular secondary objective lens (10× the working distance of 33.5 mm) and having a numerical aperture of 0.2 (Mitutoyo) was used to produce the excitation onto the samples. The laser beam, acquisition set-up and parameters were the same as for TIRF. The sample chamber was constructed by attaching two plasma clean coverslips at an 85° angle using a putty-like pressure-sensitive adhesive. Photobleaching was performed on cells fixed with paraformaldehyde and 0.2% glutaraldehyde. Image stacks using TIRF were acquired for 100 frames and ImageJ was used for data analysis as described (Latty, et al., 2018).

REFERENCES

Adams, P. D., Afonine, P. V., Bunkóczi, G., Chen, V. B., Davis, I. W., Echols, N., Headd, J. J., Hung, L. W., Kapral, G. J., Grosse-Kunstleve, R. W., Mccoy, A. J., Moriarty, N. W., Oeffner, R., Read, R. J., Richardson, D. C., Richardson, J. S., Terwilliger, T. C., & Zwart, P. H. (2010). PHENIX: A comprehensive Python-based system for macromolecular structure solution. *Acta Crystallogr. D.*, *66*, 213–221.

Akira, S., Uematsu, S., & Takeuchi, O. (2006). Pathogen recognition and innate immunity. *Cell*, *124*, 783–801.

Avbelj, M., Wolz, O. O., Fekonja, O., Benčina, M., Repič, M., Mavri, J., Krüger, J., Schärfe, C., Delmiro Garcia, M., Panter, G., Kohlbacher, O., Weber, A. N. R., & Jerala, R. (2014). Activation of lymphoma-associated MyD88 mutations via allostery-induced TIR-domain oligomerization. *Blood*, *124*, 3896–3904.

Beutler, B. (2004). Inferences, questions and possibilities in Toll-like receptor signalling. *Nature*, *430*, 257–263.

Bray, D., Levin, M. D., & Morton-Firth, C. J. (1998). Receptor clustering as a cellular mechanism to control sensitivity. *Nature*, *393*, 85–88.

Burns, K., Janssens, S., Brissoni, B., Olivos, N., Beyaert, R., & Tschopp, J. (2003). Inhibition of interleukin 1 receptor/Toll-like receptor signaling through the alternatively spliced, short form of MyD88 is due to its failure to recruit IRAK-4. *J. Exp. Med.*, *197*, 263–268.

Chen, R., Alvero, A. B., Silasi, D. A., Steffensen, K. D., & Mor, G. (2008). Cancers take their Toll–the function and regulation of Toll-like receptors in cancer cells. *Oncogene*, *27*, 225–233.

Egelman, E. H. (2000). A robust algorithm for the reconstruction of helical filaments using single-particle methods. *Ultramicroscopy*, *85*, 225–234.

Emsley, P., Lohkamp, B., Scott, W. G., & Cowtan, K. (2010). Features and development of Coot. *Acta Crystallogr. D.*, *66*, 486–501.

Fekonja, O., Benčina, M., & Jerala, R. (2012). Toll/interleukin-1 receptor domain dimers as the platform for activation and enhanced inhibition of Toll-like receptor signaling.. *J. Biol. Chem.*, *287*(37), 30993–31002.

Fischer, M. & Ehlers, M. (2008). Toll-like receptors in autoimmunity. *Ann. NY Acad. Sci.*, *1143*, 21–34.

Friedlander, T., Mayo, A. E., Tlusty, T., & Alon, U. (2015). Evolution of Bow-Tie Architectures in Biology. *PLoS Comput. Biol.*, *11*, e1004055.

Gay, N. J. & Keith, F. J. (1991). Drosophila Toll and IL-1 receptor. *Nature*, *351*, 355–356.

Gay, N. J., Symmons, M. F., Gangloff, M., & Bryant, C. E. (2014). Assembly and localization of Toll-like receptor signalling complexes. *Nat. Rev. Immunol.*, *14*, 546–558.

Goddard, T. D., Huang, C. C., Meng, E. C., Pettersen, E. F., Couch, G. S., Morris, J. H., & Ferrin, T. E. (2018). UCSF ChimeraX: Meeting modern challenges in visualization and analysis. *Protein Sci.*, *27*, 14–25.

He, S. & Scheres, S. H. W. (2017). Helical reconstruction in RELION. *J. Struc. Biol.*, *198*, 163–176.

Jaunin, F., Burns, K., Tschopp, J., Martin, T. E., & Fakan, S. (1998). Ultrastructural distribution of the death-domain-containing MyD88 protein in HeLa cells. *Exp. Cell Res.*, *243*, 67–75.

Joosten, L. A. B., Abdollahi-Roodsaz, S., Dinarello, C. A., O'Neill, L., & Netea, M. G. (2016). Toll-like receptors and chronic inflammation in rheumatic diseases: new developments. *Nat. Rev. Rheumatol.*, *12*, 344–357.

Kagan, J. C. & Medzhitov, R. (2006). Phosphoinositide-mediated adaptor recruitment controls Toll-like receptor signaling. *Cell*, *125*, 943–955.

Latty, S. L., Sakai, J., Hopkins, L., Verstak, B., Paramo, T., Berglund, N. A., Cammarota, E., Cicuta, P., Gay, N. J., Bond, P. J., Klenerman, D., & Bryant, C. E. (2018). Activation of Toll-like receptors nucleates assembly of the MyDDosome signaling hub. *eLife*, *7*, 3896.

Laue, T. M., Shah, B. D., Ridgeway, T. M., & Pelletier, S. L. (1992). Computer-Aided Interpretation of Analytical Sedimentation Data For Proteins. In S. E. Harding & J. C. Horton (Eds.), *Analytical Ultracentrifugation in Biochemistry and Polymer Science*. (pp. 90–125). Cambridge: Author.

Lin, B., Dutta, B., & Fraser, I. D. C. (2017). Systematic Investigation of Multi-TLR Sensing Identifies Regulators of Sustained Gene Activation in Macrophages. *Cell Syst.*, *5*, 25–37.

Lin, S. C., Lo, Y. C., & Wu, H. (2010). Helical assembly in the MyD88-IRAK4-IRAK2 complex in TLR/IL-1R signalling. *Nature*, *465*, 885–890.

Medzhitov, R., Preston-Hurlburt, P., Kopp, E., Stadlen, A., Chen, C., Ghosh, S., & Janeway, C. A. (1998). MyD88 is an adaptor protein in the hToll/IL-1 receptor family signaling pathways. *Mol. Cell.*, *2*, 253–258.

Mesibov, R., Ordal, G. W., & Adler, J. (1973). The range of attractant concentrations for bacterial chemotaxis and the threshold and size of response over this range. Weber law and related phenomena. *J. Gen. Physiol.*, *62*, 203–223.

Moriya, T., Saur, M., Stabrin, M., Merino, F., Voicu, H., Huang, Z., Penczek, P. A., Raunser, S., & Gatsogiannis, C. (2017). High-resolution Single Particle Analysis from Electron Cryo-microscopy Images Using SPHIRE. *Jove-J. Vis. Exp.*, 1–11.

Motshwene, P. G., Moncrieffe, M. C., Grossmann, J. G., Kao, C., Ayaluru, M., Sandercock, A. M., Robinson, C. V., Latz, E., & Gay, N. J. (2009). An oligomeric signaling platform formed by the Toll-like receptor signal transducers MyD88 and IRAK-4. *J. Biol. Chem.*, *284*, 25404–25411.

Ngo, V. N., Young, R. M., Schmitz, R., Jhavar, S., Xiao, W., Lim, K. H., Kohlhammer, H., Xu, W., Yang, Y., Zhao, H., Shaffer, A. L., Romesser, P., Wright, G., Powell, J., Rosenwald, A., Muller-Hermelink, H. K., Ott, G., Gascoyne, R. D., Connors, J. M., Rimsza, L. M., Campo, E., Jaffe, E. S., Delabie, J., Smeland, E. B., Fisher, R. I., Braziel, R. M., Tubbs, R. R., Cook, J. R., Weisenburger, D. D., Chan, W. C., & Staudt, L. M. (2011). Oncogenically active MYD88 mutations in human lymphoma. *Nature*, *470*, 115–119.

Nishiya, T., Kajita, E., Horinouchi, T., Nishimoto, A., & Miwa, S. (2007). Distinct roles of TIR and non-TIR regions in the subcellular localization and signaling properties of MyD88. *FEBS Lett.*, *581*, 3223–3229.

O'Carroll, A., Chauvin, B., Brown, J. W. P., Meagher, A., Coyle, J., Schill, J., Bhumkhar, A., Hunter, D. J. B., Ve, T., Kobe, B., Sierecki, E., & Gambin, Y. (2018). Pathological mutations differentially affect the self-assembly and polymerisation of the innate immune system signalling adaptor molecule MyD88.. *BMC biology*, *16*, 149.

Park, H. H., Logette, E., Raunser, S., Cuenin, S., Walz, T., Tschopp, J., & Wu, H. (2007). Death domain assembly mechanism revealed by crystal structure of the oligomeric PIDDosome core complex. *Cell*, *128*, 533–546.

Pettersen, E. F., Goddard, T. D., Huang, C. C., Couch, G. S., Greenblatt, D. M., Meng, E. C., & Ferrin, T. E. (2004). UCSF Chimera–A visualization system for exploratory research and analysis. *J. Comput. Chem.*, *25*, 1605–1612.

Ponjavic, A., McColl, J., Carr, A. R., Santos, A. M., Kulenkampff, K., Lippert, A., Davis, S. J., Klenerman, D., & Lee, S. F. (2018). Single-Molecule Light-Sheet Imaging of Suspended T Cells.. *Biophys J*, *114*, 2200–2211.

Punjani, A., Rubinstein, J. L., Fleet, D. J., & Brubaker, M. A. (2017). CryoSPARC: algorithms for rapid unsupervised cryo-EM structure determination. *Nat. Methods*, *14*, 290–296.

Scheres, S. H. W. (2012). RELION: implementation of a Bayesian approach to cryo-EM structure determination. *J. Struc. Biol.*, *180*, 519–530.

Schuck, P. (2000). Size-distribution analysis of macromolecules by sedimentation velocity ultracentrifugation and Lamm equation modeling. *Biophys. J.*, *78*, 1606–19.

Schuck, P. (2003). On the analysis of protein self-association by sedimentation velocity analytical ultracentrifugation. *Anal. Biochem.*, *320*, 104–124.

Seong, S. Y. & Matzinger, P. (2004). Hydrophobicity: an ancient damage-associated molecular pattern that initiates innate immune responses. *Nat. Rev. Immunol.*, *4*, 469–478.

Suzuki, N., Suzuki, S., Duncan, G. S., Millar, D. G., Wada, T., Mirtsos, C., Takada, H., Wakeham, A., Itie, A., Li, S., Penninger, J. M., Wesche, H., Ohashi, P. S., Mak, T. W., & Yeh, W. C. (2002). Severe impairment of interleukin-1 and Toll-like receptor signalling in mice lacking IRAK-4. *Nature*, *416*, 750–756.

Treon, S. P., Xu, L., Yang, G., Zhou, Y., Liu, X., Cao, Y., Sheehy, P., Manning, R. J., Patterson, C. J., Tripsas, C., Arcaini, L., Pinkus, G. S., Rodig, S. J., Sohani, A. R., Harris, N. L., Laramie, J. M., Skifter, D. A., Lincoln, S. E., & Hunter, Z. R. (2012). MYD88 L265P somatic mutation in Waldenström's macroglobulinemia. *New Engl. J. Med.*, *367*, 826–833.

Vagin, A. A. & Isupov, M. N. (2001). Spherically averaged phased translation function and its application to the search for molecules and fragments in electron-density maps. *Acta Crystallogr. D.*, *57*, 1451–1456.

Ve, T., Vajjhala, P. R., Hedger, A., Croll, T., DiMaio, F., Horsefield, S., Yu, X., Lavrencic, P., Hassan, Z., Morgan, G. P., Mansell, A., Mobli, M., O'Carroll, A., Chauvin, B., Gambin, Y., Sierecki, E., Landsberg, M. J., Stacey, K. J., Egelman, E. H., & Kobe, B. (2017). Structural basis of TIR-domain-assembly formation in MAL- and MyD88-dependent TLR4 signalling. *Nat. Struc. Mol. Biol.*, *267*, 15836.

Vyncke, L., Bovijn, C., Pauwels, E., Van Acker, T., Ruyssinck, E., Burg, E., Tavernier, J., & Peelman, F. (2016). Reconstructing the TIR Side of the Myddosome: A Paradigm for TIR-TIR Interactions. *Structure*, *24*, 437–447.

Wang, Z., Hryc, C. F., Bammes, B., Afonine, P. V., Jakana, J., Chen, D. H., Liu, X., Baker, M. L., Kao, C., Ludtke, S. J., Schmid, M. F., Adams, P. D., & Chiu, W. (2014). An atomic model of brome mosaic virus using direct electron detection and real-space optimization. *Nat. Commun.*, *5*, 4808.

Weber, C. H. & Vincenz, C. (2001). The death domain superfamily: a tale of two interfaces?. *Trends Biochem. Sci*, *26*, 475–481.

Wesche, H., Henzel, W. J., Shillinglaw, W., Li, S., & Cao, Z. (1997). MyD88: an adapter that recruits IRAK to the IL-1 receptor complex. *Immunity*, *7*, 837–847.

Zhang, K. (2016). Gctf: Real-time CTF determination and correction. *J. Struc. Biol.*, *193*, 1–12.

Zheng, S. Q., Palovcak, E., Armache, J. P., Verba, K. A., Cheng, Y., & Agard, D. A. (2017). MotionCor2: anisotropic correction of beam-induced motion for improved cryo-electron microscopy. *Nat. Methods*, *14*, 331–332.

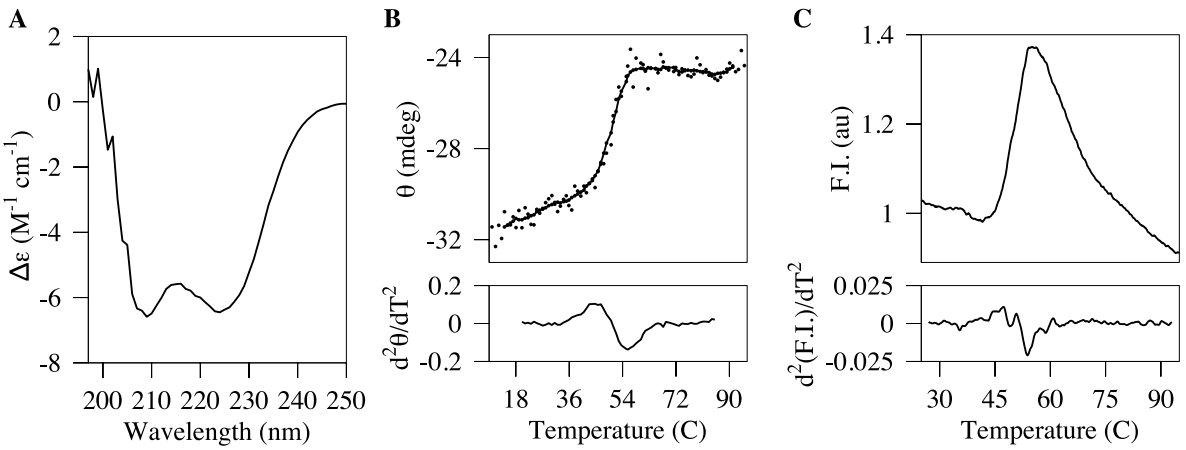

Figure S1 Characterization of the hMyD88^{DD} oligomer. Related to Figure 1, Figure 2 and STAR Methods section 'Circular dichroism spectroscopy and differential scanning fluorometry' (**A**) The far-UV circular dichroism spectrum of the oligomeric MyD88^{DD} displays characteristic peaks reflective of α-helical secondary structure at 209 nm 223 nm respectively. Thermal denaturation profiles measured by monitoring the decrease of ordered secondary structure content using circular dichroism (**B**) in the far-UV (222 nm) and the fluorescence of SPYRO orange (**C**) gives T_m values of 55.7 °C and 53.4 °C.

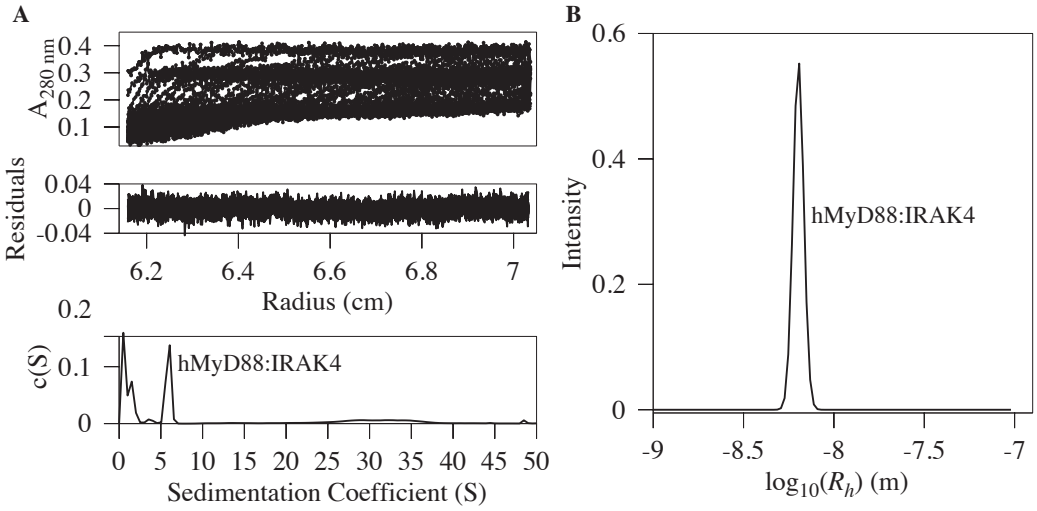

Figure S2 MyD88^{DD} filaments interact with IRAK4^{DD}. Related to Figure 4. (**A**) Formation of the hMyD88^{DD}-IRAK4^{DD} complex from helical hMyD88^{DD} filaments. (**B**) Dynamic light scattering distribution of the hMyD88^{DD}-IRAK4^{DD} complex purified by S200 size exclusion chromatography.

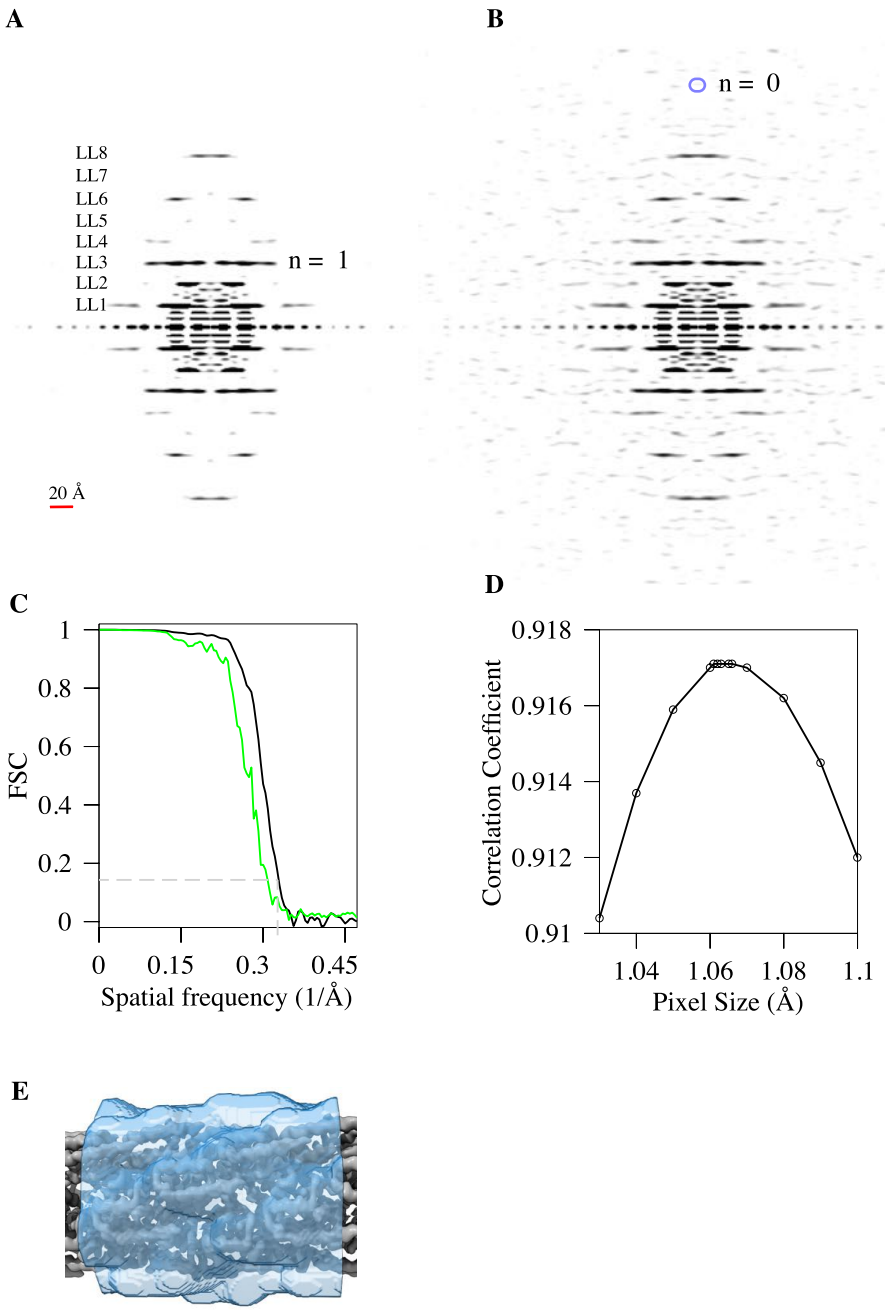

Figure S3 Reconstruction of the MyD88^{DD} filament. Related to Figure 2 and Figure 3. Averaged power spectrum of hMyD88^{DD} filaments display layer lines (LL) which are typical of objects possessing helical symmetry. (**A**) The first eight layer lines (LL1–LL8) are shown and the Bessel order ($n = 1$) for LL3. (**B**) The first meridional line for which the Bessel order is zero ($n = 0$), which represents the helical rise is shown circled in blue. (**C**) Fourier shell correlation. Masked (black), unmasked (green). The dotted line depicts the point where FSC = 0.143 and the corresponding resolution. (**D**) Pixel size at the specimen level. Plot of the correlation coefficient for the fit between the three-dimensional coordinates of MyD88^{DD} (PDB code 3MOP) and the cryo-EM map as a function of voxel size. (**E**) Reconstructed hMyD88^{DD} filament and the soft mask used in post-processing.

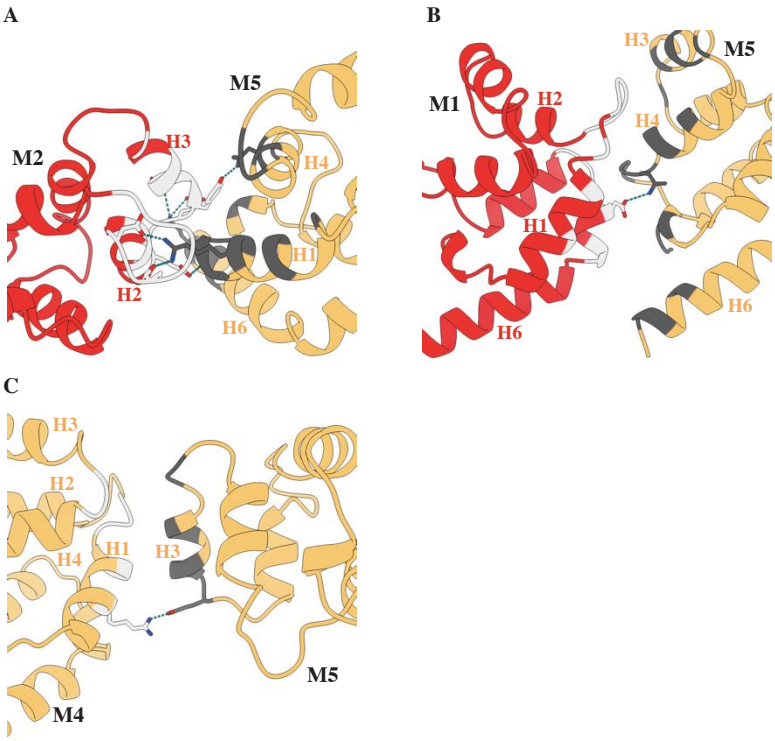

Figure S4 Interfaces of the MyD88^{DD} filament. Related to Figure 3. Type I (**A**), II (**B**), and III (**C**), interfaces seen in the hMyD88^{DD} filament. The respective *a* or *b* interaction surfaces are displayed in dark- and light-grey respectively. Details of the actual residues involved are given in Table S1.

Table S1 Typical interfacial residues in the MyD88^{DD} filament. Related to Figure 3. Residues in the type I, II and III interface of the MyD88 death domain filament. Residues involved in hydrogen bonds and salt-bridges are indicated by H and S respectively.

Type I		Type II		Type III	
a	**b**	**a**	**b**	**a**	**b**
A23	R40	S19	R32	E57^{S}	R32^{S}
L25	T41^{H}	L20	F36	Y58	L35
N26^{H}	Q42	P21	V39	L59	F3
M27	V43	A23	T41	E60	N38
R28^{H}	A44^{H}	F56	Q42	R62	V39
R30	A45	E60	V43	Q63	R40
R31^{H,S}	D46^{S}	Q63	A44	T66	A68
S34	T48^{H}	L64	A45	Q67	D69
L35	A49	Q67	L96		E104
N38	Q52^{H}	R73	G97		
A68	D55	D76	R98		
D69	F56	A77	D99		
R73	E57^{S}	Q79^{S}	D100^{S}		
D76^{H,S}	Y58^{H}	G80	L103		
Q79	L59	R81	E104^{H}		
K115	E60	P82			
Y116	I61	Y116^{H}			
K119^{S}	R62^{S}	K119			
	E65	Q120			

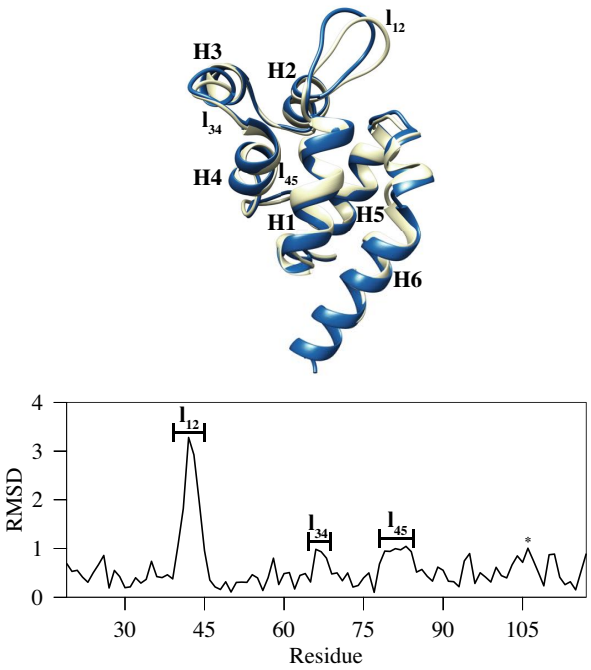

Figure S5 Superposition of MyD88^{DD} determined by cryo-EM and X-ray crystallography. Related to Figure 3. Structure of MyD88^{DD} from the death domain filament (blue) and the ternary MyD88-IRAK4-IRAK2 Myddosome (yellow). The r.m.s.d. across all atom pairs is 0.76 Å. The largest differences occur in the loop regions connecting the α-helices H1–H2 (l_{12}), H3–H4 (l_{34}), H4–H5 (l_{45}) and a break in H6 at G106(∗).

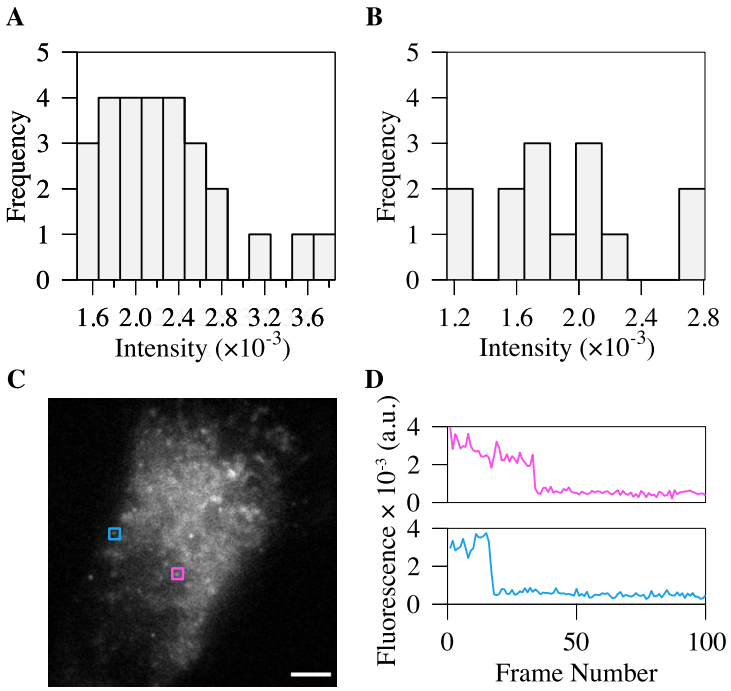

Figure S6 MyDDosome formation in cells. Related to Figure 5. Histograms of the intensity distributions for GFP-MyD88 in unstimulated (**A**) and stimulated (**B**) virally transduced MyD88$^{-/-}$ bone derived macrophage macrophages.Determination of monomeric MyD88 intensity by photobleaching. The locations indicated by coloured squares (**C**) were bleached and the intensity trajectory after bleaching is shown (**D**). At these locations, GFP-MyD88 bleaches in a single step suggesting that the protein is monomeric. The length of the scale bar is 5 µm.